



**HAL**  
open science

# Electrostatic Spacecraft Potential Structure and Wake Formation Effects for Characterization of Cold Ion Beams in the Earth's Magnetosphere

S. Toledo-Redondo, B. Lavraud, S. A. Fuselier, M. André, Yu. V. Khotyaintsev, R. Nakamura, C. P. Escoubet, W. Y. Li, K. Torkar, F. Cipriani, et al.

## ► To cite this version:

S. Toledo-Redondo, B. Lavraud, S. A. Fuselier, M. André, Yu. V. Khotyaintsev, et al.. Electrostatic Spacecraft Potential Structure and Wake Formation Effects for Characterization of Cold Ion Beams in the Earth's Magnetosphere. *Journal of Geophysical Research Space Physics*, 2019, 124, pp.10,048-10,062. 10.1029/2019JA027145 . insu-03674379

**HAL Id: insu-03674379**

**<https://insu.hal.science/insu-03674379>**

Submitted on 20 May 2022

**HAL** is a multi-disciplinary open access archive for the deposit and dissemination of scientific research documents, whether they are published or not. The documents may come from teaching and research institutions in France or abroad, or from public or private research centers.

L'archive ouverte pluridisciplinaire **HAL**, est destinée au dépôt et à la diffusion de documents scientifiques de niveau recherche, publiés ou non, émanant des établissements d'enseignement et de recherche français ou étrangers, des laboratoires publics ou privés.

Copyright

# JGR Space Physics

## RESEARCH ARTICLE

10.1029/2019JA027145

### Key Points:

- The modeled MMS spacecraft electrostatic potential distribution deviates from spherical because of the electric field booms
- Measurements by particle detectors in the magnetosphere are strongly affected and biased by the complex potential structure
- Cold ion beam properties are constrained by characterizing the ion wake and using a combination of particle and electric field measurements

### Correspondence to:

S. Toledo-Redondo,  
sergiotr@ugr.es

### Citation:

Toledo-Redondo, S., Lavraud, B., Fuselier, S. A., André, M., Khotyaintsev, Y. V., Nakamura, N., et al. (2019). Electrostatic spacecraft potential structure and wake formation effects for characterization of cold ion beams in the Earth's magnetosphere. *Journal of Geophysical Research: Space Physics*, 124, 10,048–10,062. <https://doi.org/10.1029/2019JA027145>

Received 10 JUL 2019

Accepted 5 SEP 2019

Accepted article online 21 OCT 2019

Published online 11 DEC 2019

## Electrostatic Spacecraft Potential Structure and Wake Formation Effects for Characterization of Cold Ion Beams in the Earth's Magnetosphere

S. Toledo-Redondo<sup>1</sup> , B. Lavraud<sup>1</sup> , S. A. Fuselier<sup>2,3</sup> , M. André<sup>4</sup> , Yu. V. Khotyaintsev<sup>4</sup> , R. Nakamura<sup>5</sup> , C. P. Escoubet<sup>6</sup>, W. Y. Li<sup>7</sup>, K. Torkar<sup>5</sup> , F. Cipriani<sup>6</sup>, A. C. Barrie<sup>8</sup> , B. Giles<sup>8</sup> , T. E. Moore<sup>8</sup> , D. Gershman<sup>8</sup> , P.-A. Lindqvist<sup>9</sup> , R. E. Ergun<sup>1,10</sup> , C. T. Russell<sup>1,11</sup> , and J. L. Burch<sup>2</sup> 

<sup>1</sup>Institut de Recherche en Astrophysique et Planétologie, Université de Toulouse, CNRS, UPS, CNES, Toulouse, France,

<sup>2</sup>Southwest Research Institute, San Antonio, TX, USA, <sup>3</sup>Department of Physics and Astronomy, University of Texas at San Antonio, San Antonio, TX, USA, <sup>4</sup>Swedish Institute of Space Physics, Uppsala, Sweden, <sup>5</sup>Space Research Institute, Austrian Academy of Sciences, Graz, Austria, <sup>6</sup>European Space Agency, ESA/ESTEC, Noordwijk, Netherlands, <sup>7</sup>State Key Laboratory of Space Weather, National Space Science Center, Chinese Academy of Sciences, Beijing, China, <sup>8</sup>NASA Goddard Space Flight Center, Greenbelt, MD, USA, <sup>9</sup>Department of Space and Plasma Physics, Royal Institute of Technology, Stockholm, Sweden, <sup>10</sup>Laboratory of Atmospheric and Space Physics, University of Colorado Boulder, Boulder, CO, USA, <sup>11</sup>Department of Earth and Space Sciences, University of California, Los Angeles, CA, USA

**Abstract** Cold plasma (up to few tens of electron volts) of ionospheric origin is present most of the time, in most of the regions of the Earth's magnetosphere. However, characterizing it using in situ measurements is difficult, owing to spacecraft electrostatic charging, as often this charging is at levels comparable to or even higher than the equivalent energy of the cold plasma. To overcome this difficulty, active potential control devices are usually placed on spacecraft that artificially reduce spacecraft charging. The electrostatic potential structure around the spacecraft is often assumed to be spherically symmetric, and corrections are applied to the measured particle distribution functions. In this work, we show that large deviations from the spherical model are present, owing to the presence of long electric field booms. We show examples using Magnetospheric MultiScale spacecraft measurements of the electrostatic potential structure and its effect on the measurement of cold ion beams. Overall, we find that particle detectors underestimate the cold ion density under certain conditions, even when their bulk kinetic energy exceeds the equivalent spacecraft potential energy and the ion beam reaches the spacecraft. Active potential control helps in reducing this unwanted effect, but we show one event with large cold ion density ( $\sim 10 \text{ cm}^{-3}$ ) where particle detectors provide density estimates a factor of 3–5 below the density estimated from the plasma frequency. Understanding these wake effects indirectly constrains some properties of the magnetospheric cold ion component, such as their drift energy, direction, and temperature.

**Plain Language Summary** The near-Earth space environment is filled with plasma, that is, ionized gas that interacts with electromagnetic fields. Owing to its relative accessibility, it constitutes an invaluable laboratory for understanding how plasmas behave in nature. Many spacecraft missions have been launched with the purpose of studying space plasmas since the 1960s, when the space era began. They carry in situ instrumentation capable of measuring the properties of electric and magnetic fields, as well as the properties of ions and electrons. One problem these missions encounter is that the spacecraft produce their own electromagnetic fields that locally interact with the plasma and modify their properties. In this work, we quantify the effects of electric field booms mounted on spacecraft, which have length scales much larger than the spacecraft itself. The electromagnetic properties of these spacecraft booms strongly affect the detection and characterization of cold plasma, that is, low-temperature plasma. Cold plasma in the near-Earth space environment originates in the ionosphere, populates the whole magnetosphere, and constitutes the most abundant magnetospheric population.

### 1. Introduction

The Earth's magnetosphere is composed of a mixture of hot (thermal energy of few to several kiloelectron volts) and cold (thermal energy of up to tens of electron volts) ions. Typical hot magnetospheric populations

are, for instance, the ring current and the plasma sheet. The cold populations originate in the ionosphere, via various mechanisms such as ionospheric outflows at high latitudes (e.g., Yau & Andre, 1997, and references therein) and plasmaspheric winds and drainage plumes at low and middle latitudes (e.g., Dandouras, 2013; Darrouzet et al., 2008). These cold ions are often a mixture of protons and heavier species such as  $\text{He}^+$  and  $\text{O}^+$  (e.g., Fuselier et al., 2017) and are accompanied by cold electrons (e.g., Toledo-Redondo et al., 2017). The cold plasmas of ionospheric origin are, together with the solar wind, a major source of magnetospheric plasma (Chappell, 2015).

In situ spacecraft measurements of space plasmas in the near-Earth environment became available during the first space missions in the early 1960s. A prominent issue when performing these measurements in low-density plasmas, that is, in regions above the ionosphere, is spacecraft charging. Solar extreme ultraviolet radiation impinging on the metal parts of the spacecraft excite photoelectrons that detach from the illuminated surfaces. This effect generates a net current flowing from the ambient plasma toward the spacecraft, which results in a positive spacecraft charging ( $V_{sc}$ ) with respect to the ambient plasma. For positive potentials, as is often the case in the magnetosphere, the electrostatic potential structure around the spacecraft repels cold ions and attracts cold electrons. This results in an ion rarefaction or ion wake behind the spacecraft, owing to the lower mobility of ions. Spacecraft in the Earth's magnetosphere typically charge up to few tens of volts. When this voltage is reached, the photoelectron current is balanced with other currents, such as the electron and ion currents (e.g., Andriopoulou et al., 2015; Pedersen et al., 1984). The plasma to spacecraft potential is routinely measured by electric field instruments on board these spacecraft, which are based on a double-probe technique (e.g., Gustafsson et al., 1997; Lindqvist et al., 2014).

Particle measurements are affected by the electrostatic potential structure around the spacecraft (Engwall et al., 2006; Olsen, 1982; Su et al., 1998). Ambient electrons experience a gain in energy when approaching the electron detectors (Szita et al., 2001). The potential structure that forms around the spacecraft is often assumed to have spherical symmetry. Under this assumption, a correction is applied to detected electrons to account for the effect of the spacecraft potential, which consists of subtracting  $V_{sc}$  times the electron charge from the measured energy. In addition, the spacecraft attracts back emitted photoelectrons with outflowing energies below the equivalent  $V_{sc}$ . These photoelectrons are much more abundant than ambient electrons in the magnetosphere and result in high count rates in the lower energy channels of electron detectors. A common practice to mitigate this unwanted effect is to discard the information coming from the energy channels with energies below the equivalent  $V_{sc}$  (Lavraud & Larson, 2016; McFadden et al., 2008). In the case of ions, they encounter the potential barrier and loose energy before reaching the ion detectors mounted on the spacecraft body. The correction is analogous to that for electrons, that is, one assumes spherical symmetry of the potential, and the measured energy is corrected by adding  $V_{sc}$  times the ion charge. Ambient ions with kinetic energy below the equivalent  $V_{sc}$  are not able to reach the ion particle detectors.

The electrostatic potential structure around the spacecraft has a strong impact on measurement and characterization of the magnetospheric ion component of ionospheric origin. Typical thermal energies of such ions are usually below  $q_{ic}V_{sc}$ , where  $q_{ic}$  is the cold ion charge, and they are measured by ion detectors only when the energy associated with their bulk velocity relative to the spacecraft velocity becomes larger than  $q_{ic}V_{sc}$  (e.g., Toledo-Redondo et al., 2017). Various mechanisms, such as motion of the Earth's magnetopause, magnetospheric convection, or low-frequency waves (e.g., Hirahara et al., 2004; Sauvaud et al., 2001; Toledo-Redondo et al., 2015), to name a few, can accelerate the ions relative to the spacecraft to energies above  $V_{sc}$ , and only then do the cold ions become visible. However, during most of the time, the cold ions remain invisible to ion detectors.

In addition, when cold ions are unable to reach the spacecraft and are deflected by the spacecraft potential, a cold ion wake is generated around the spacecraft (Engwall et al., 2006). The characteristic spatial scale of the spacecraft potential structure can extend up to the Debye length-scale (few hundreds of meters in the magnetosphere), and it is screened by the plasma at larger scales. Therefore, a rarefaction of ions is formed behind the spacecraft, locally generating an electric field commonly referred to as the wake electric field ( $\mathbf{E}_{wake}$ ). Similar problems of wake formation occur in sounding rockets when traversing the ionosphere (Paulsson et al., 2018) or in other planetary environments (Bergman et al., 2018). The shape and size of these wakes is modified by the presence of booms that are charged to spacecraft potential levels, which often measure several to tens of meters and have a major effect on the potential structure around the spacecraft (Cully et al., 2007; Miyake & Usui, 2016; Miyake et al., 2013).

Engwall et al. (2006) developed an innovative method to indirectly infer the flux of invisible cold ions based on the properties of  $E_{\text{wake}}$ . This technique revealed an increased number density of cold ions of ionospheric origin in the Earth's magnetosphere (André & Cully, 2012; Engwall et al., 2009). Statistical surveys based on particle instruments provide lower densities (e.g., Chen & Moore, 2006; Fuselier et al., 2017; Lee & Angelopoulos, 2014) of the cold ionospheric component than indirect methods.

A way to mitigate the effects of spacecraft charging is to include an instrument capable of expelling ions, or ion emitter (e.g., Torkar et al., 2001, 2014). The instrument generates an additional current that counteracts the photoelectron current and results in lowering the spacecraft potential to a few volts. This technique is beneficial for measuring both cold electrons and cold ions.

In this work, we present Magnetospheric MultiScale (MMS; Burch et al., 2015) spacecraft measurements of the Earth's magnetosphere, when the ionospheric cold ion component is present. We demonstrate that the electrostatic potential structure around the spacecraft cannot be assumed to be spherical for particle measurements correction, due to the effect of long electric field booms. These booms are charged to the same potential as the spacecraft body, and thus, they extend the spacecraft potential very far away from the spacecraft body. In the vicinity of the boom, the electric field is directed radially away from the boom, and it deflects the cold ions moving along the booms toward the spacecraft, creating a void in the cold ions in the direction of the booms. Section 2 shows the results of modeling the MMS spacecraft potential structure. Section 3 first gives an overview of the event shown to illustrate the effects of the spacecraft potential structure when measuring cold ions and the electric field. Then, it discusses in detail the measurements made by the Fast Plasma Investigation (FPI; Pollock et al., 2016), the Hot Plasma Composition Analyzer (HPCA; Young et al., 2014), and the Spin Double Probes (SDP; Lindqvist et al., 2014), under various ambient plasma conditions and during periods with and without the ASPOC (Active Spacecraft Potential Control) operation (Torkar et al., 2014). Finally, in section 4, we discuss and summarize the main findings and implications of this work.

## 2. MMS Spacecraft Potential Structure Modeling

MMS was launched in March 2015 and successfully inserted into an equatorial, highly elliptical orbit around Earth. It is composed of four identical spin-stabilized ( $\sim 19.5$ -s period) spacecraft flying in close (from 10 km to few tens of kilometers) tetrahedron formation, to disentangle temporal and spatial changes in the plasma. Its primary focus is to study magnetic reconnection processes between the solar wind and the Earth's magnetosphere and in the magnetotail. The spacecraft design is octagonal (i.e., close to cylindrical) with a radius of  $\sim 2$  m, with the aim of minimizing changes in solar irradiation as they spin. Changes in the effective surface illuminated would result in variations of the amount of energy the solar panels receive, and would produce a varying spacecraft potential owing to a varying photoelectron current production. Nevertheless, cylindrical symmetry cannot be accomplished: there are four wire booms deployed in the spin plane (60 m each) that host electric field probes at their edges (Lindqvist et al., 2014), plus two axial semirigid booms (12.5 m each boom plus 2.25 m each antenna; Ergun et al., 2014). The spin axis is slightly shifted from Geocentric Solar Ecliptic System (GSE) Z axis ( $\sim 3^\circ$ ) to avoid shadowing the probes by the spacecraft body. In addition, there are two more booms (5 m each) that host the Flux Gate Magnetometers (FGM) and the Search Coil Magnetometers (SCM; Le Contel et al., 2014; Russell et al., 2014). In this work, we focus on the effect of the long (60 m) wire booms on the potential structure, although similar but smaller effects, owing to their shorter length, are expected as well for the axial and magnetometer booms.

A model of the electrostatic potential structure for MMS (Cipriani et al., 2018) has been developed using the Spacecraft Plasma Interaction Software (SPIS; Roussel et al., 2008). The SPIS numerical scheme is based on a Particle in Cell approach to solve the 3-D Vlasov-Poisson equation, with a coupled dynamic current solver at the spacecraft surface that computes the surface currents. Spacecraft photoelectrons and secondary electrons excited from ambient electrons are produced as a function of illumination and ambient plasma conditions. Therefore, the code self-consistently computes the currents between the spacecraft and the ambient plasma, providing a picture of the electromagnetic fields in the vicinity of the spacecraft. A simplified 3-D model of the MMS spacecraft was created, which accounts for the largest features such as spin, axial and magnetometer booms, as well as representative spacecraft surface materials (full description in Cipriani, 2016), but not for small-scale details such as bolts or fasteners. In this model, the SDP spherical probes and Axial Double Probes (ADP) were also omitted. A relatively crude mesh resolution was chosen in order to

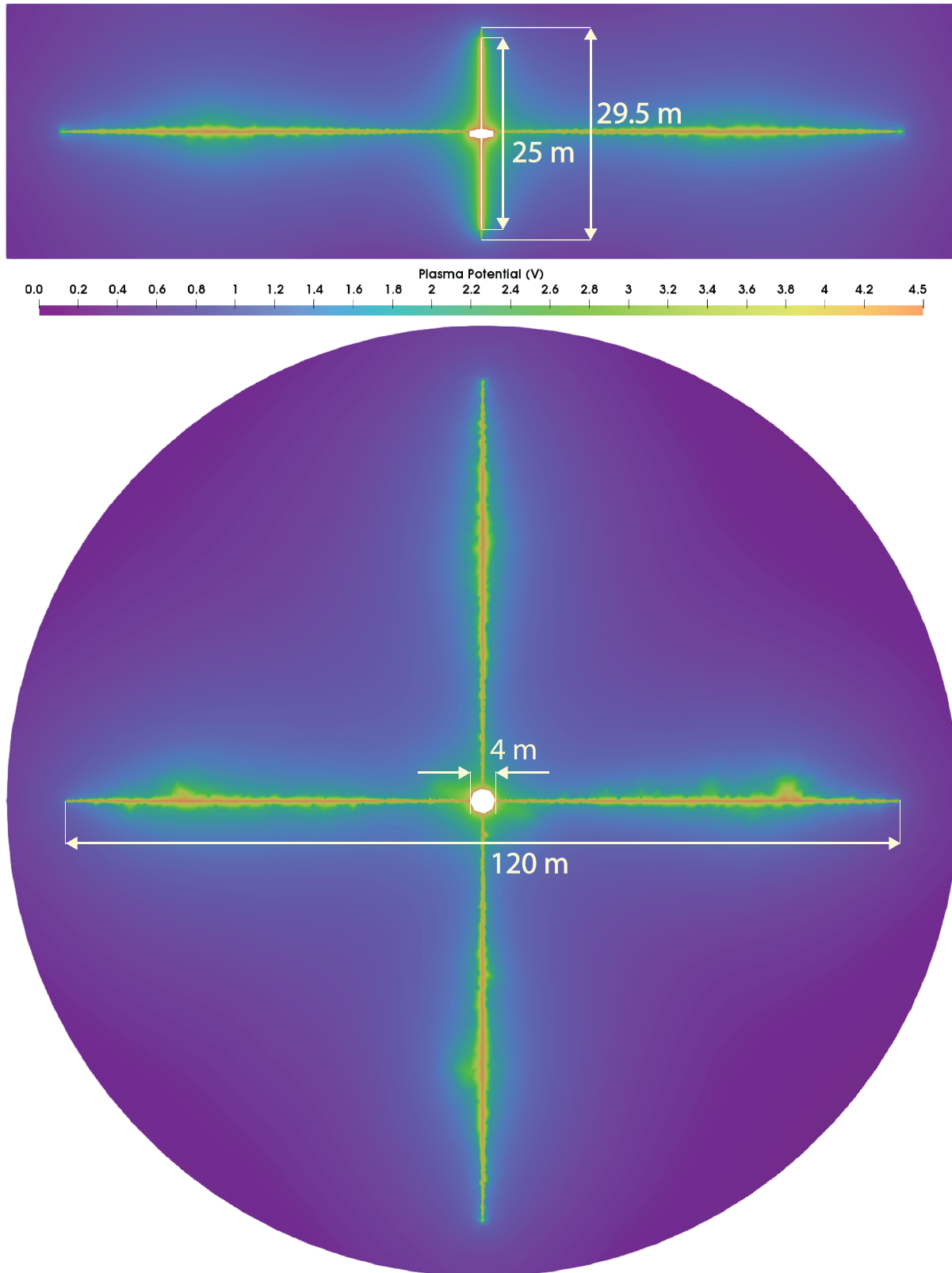


**Figure 1.** Simulated plasma potential structure around Magnetospheric MultiScale spacecraft body, including booms. The small-scale potential structures around the booms are caused by the mesh resolution and are not real. The conducting spin-plane wire booms and axial booms extend spacecraft potential charging far away from the spacecraft. (top) XZ plane in spacecraft coordinates. (bottom) XY plane in spacecraft coordinates.

reduce the computing time while still providing accurate spacecraft potential values. The resulting potential structure for given conditions in the magnetosphere are presented in Figure 1. In this run, typical magnetospheric conditions are assumed: plasma density  $n_e = n_i = 0.6 \text{ cm}^{-3}$ , and  $T_i = T_e = 0.5 \text{ keV}$ . The resulting spacecraft potential is  $V_{sc} = 4.6 \text{ V}$ . The spacecraft is considered to be fixed in space during the run, that is, the spin motion is not included in the model. This is justified because the dynamics of charging the spacecraft are much faster than the spin period ( $\sim 20 \text{ s}$ ).

Figure 1 shows that presence of the wire booms has a major effect of the electrostatic potential structure around the spacecraft, and that the electromagnetic fields that ions and electrons experience when approaching the spacecraft differ from an often-assumed spherical potential centered around the spacecraft body. It is worth remembering here that the maximum length-scale of the MMS spacecraft is 120 m tip-to-tip, that is, below the Debye length-scale  $L_D = (\epsilon_0 K T_e / n_e q_e^2)^{1/2} \simeq 215 \text{ m}$  for typical magnetospheric conditions, where  $\epsilon_0$  is the vacuum dielectric permittivity,  $K$  is the Boltzmann constant, and  $q_e$  is the magnitude of the electron charge.

### 3. In Situ Observations of the Cold Ion Component

On 28 December 2016, at about 11:28 UT, the MMS fleet was in the dayside magnetosphere close to the magnetopause, at [11.5, 1.7, 1.3] Earth radii in GSE coordinates. Figure 2a shows the measured magnetic field ( $\mathbf{B}$ ) in GSE coordinates. The yellow-shaded region corresponds to roughly one spin time interval, and it will be shown in detail in Figure 3. Figure 2b is a wavelet spectrogram of the  $\mathbf{B}$  field, presented here to show that no clear periodic signal multiples of the spin frequency are observed by FGM. Figure 2c shows the measured electric field ( $\mathbf{E}$ ) by the spin probes in GSE coordinates, featuring a periodic signal. The wavelet spectrogram of Figure 2d reveals a persistent tone within the magnetosphere interval (11:27:40–11:30:10 UT) at  $\sim 0.2 \text{ Hz}$ . This frequency roughly corresponds to 4 times the spin frequency ( $f_s \simeq 0.05 \text{ Hz}$ ). Figure 2e shows estimates for the plasma density from three different sources: the FPI Dual Ion spectrometers (FPI-DIS) instrument ( $n_i$ , black line), the FPI Dual Electron Spectrometer (FPI-DES) instrument ( $n_e$ , green line) and inferred from the plasma frequency ( $n_{ip} = \omega_{ip}^2 \epsilon_0 m_e / q_e^2$ , where  $\omega_{ip}$  is the plasma angular frequency,  $m_e$  is the electron mass and  $q_e$  corresponds to the magnitude of the electron charge) measured from fluctuations in the electric field (red). The plasma frequency indicates an average plasma density of  $1 - 2 \text{ cm}^{-3}$ , and corresponds to the most reliable measurement of the true plasma density. The density detected by the ion instrument jumps between  $0.2$  and  $2 \text{ cm}^{-3}$  periodically, with the same period as the observed low-frequency fluctuations in  $\mathbf{E}$ . The electron instrument does not observe the periodic fluctuations, and measures a density significantly lower, below  $0.5 \text{ cm}^{-3}$  during most of the time interval. Figure 2f shows an ion omnidirectional spectrogram in differential energy flux (dEF) units, measured by FPI-DIS. Before 11:27:35 UT, an ion component consistent with magnetosheath plasma is observed. After that time, two populations at different energy ranges are detected by FPI-DIS. One is commonly referred to as the ring current, with characteristic energies of the order of several keV. The other population is observed in the 10–20 eV energy range, and periodic gaps in the detection are observed, consistent with  $n_i$  periodic fluctuations. The cold ion component is not detected in the time interval 11:28:25–11:28:37 UT. We identify the cold ion component as a cold proton beam of ionospheric origin. Finally, a faint third component is observed at energies of  $\sim 100 \text{ eV}$ . The Hot Plasma Composition Analyzer (HPCA) instrument resolves the ion mass and indicates that this third component corresponds to cold  $\text{He}^+$  (not shown). HPCA shows that the  $\text{He}^+$  number density is roughly 2 orders of magnitude below the proton density, and therefore does not significantly contribute to the overall plasma density. Simultaneous observations of cold  $\text{H}^+$  and  $\text{He}^+$  in the energy and density range mentioned are consistent with local observation of the plasmaspheric drainage plume (Darrouzet et al., 2008). MMS1, MMS2, MMS3, and MMS4 were separated by one another by about 10 km, and all spacecraft observed the same features. The gaps in cold proton detection do not occur at the same time among different spacecraft. All these indications let us conclude that: (1) the cold ion component is periodically deflected by the potential structure and prevented from reaching FPI; (2) the observed  $\mathbf{E}$  field periodicity at  $\sim 0.2 \text{ Hz}$  does not correspond to natural fluctuations of the ambient plasma but is caused by an intermittent wake electric field ( $\mathbf{E}_{\text{wake}}$ ) in the vicinity of the spacecraft. This wake is likely due to the deflection of cold ions by the electric field booms potential structure; (3) the plasma density is  $1 - 2 \text{ cm}^{-3}$ , as indicated by  $n_p$  and  $n_i$  when the cold proton component is detected by FPI-DIS. Figure 2g shows the electron omnidirectional spectrogram in dEF units. The spacecraft potential ( $V_{sc}$ ) is plotted on top using a white line. In the magnetosphere region, two electron populations can be distinguished: ring current electrons with energies of few keV plus a cold electron component slightly above

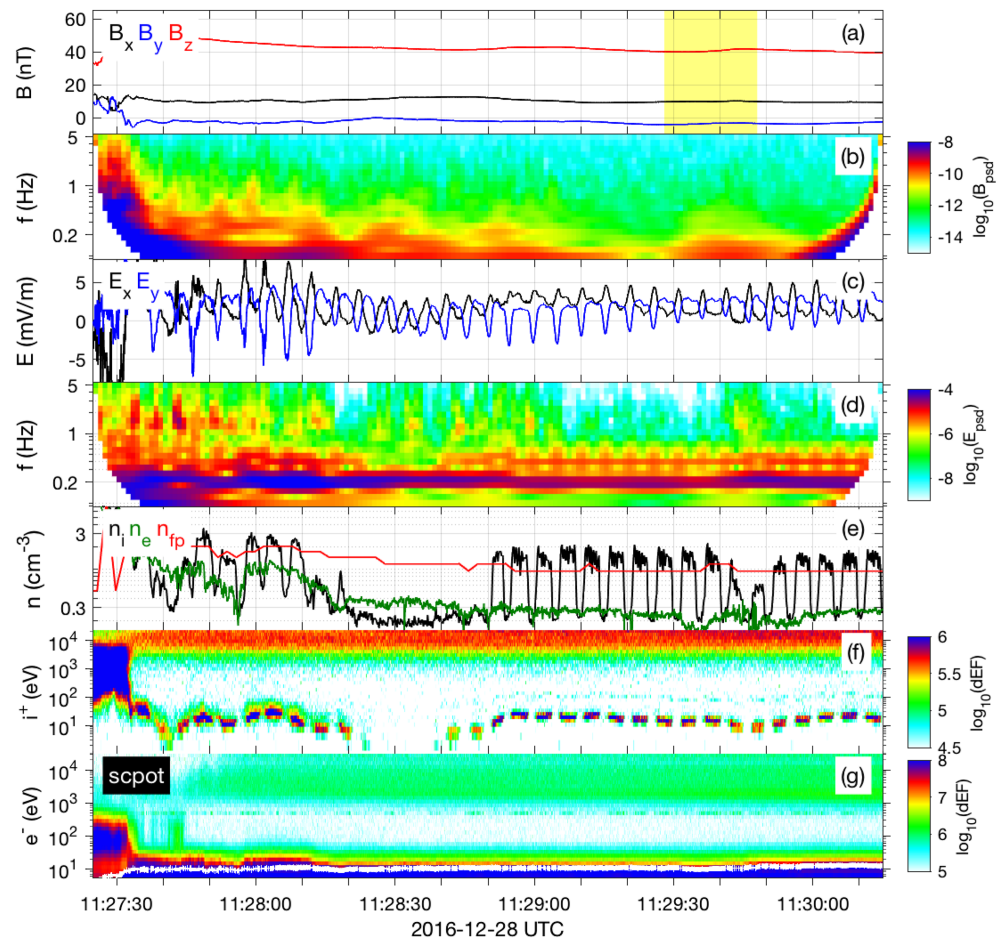


**Figure 2.** MMS1 measurements in the magnetosphere near the magnetopause, [11.5, 1.7, 1.3] Earth radii in GSE coordinates. (a) Magnetic field in GSE coordinates. The time interval of Figure 3 is marked in yellow. (b) Magnetic field spectrogram in  $T^2/\text{Hz}$ . (c) Electric field in GSE coordinates. (d) Electric field spectrogram,  $\text{V}^2 \cdot \text{m}^{-2} \cdot \text{Hz}^{-1}$ . (e) (black) Plasma density observed by FPI-DIS ( $n_i$ ), (green) FPI-DES ( $n_e$ ), (red) and inferred from plasma frequency line observed by the electric field instrument ( $n_{fp}$ ). (f) FPI ion spectrogram in differential energy flux (dEF),  $\text{keV}/(\text{cm}^2 \text{ s sr keV})$ . (g) (color) FPI electron spectrogram in differential energy flux (dEF),  $\text{keV}/(\text{cm}^2 \text{ s sr keV})$ , (white) spacecraft potential ( $V_{sc}$ ), V. MMS = Magnetospheric MultiScale; GSE = Geocentric Solar Ecliptic System; FPI = Fast Plasma Investigation; FPI-DIS = FPI Dual Ion spectrometers; FPI-DES = FPI Dual Electron spectrometers.

the spacecraft potential ( $\sim 20$  eV). Below  $V_{sc}$ , the measurements are contaminated by spacecraft photoelectrons and are not accounted for when computing the electron moments. However, cold electrons from the plasmaspheric plume are also dropped from the moment calculation, hence the low  $n_e$  values.

### 3.1. Effects on the Fast Plasma Investigation and on the Spin Dual Probes Measurements

In this section, we focus on the time interval marked in yellow in Figure 2a, which is presented in detail in Figure 3. It corresponds to 20 s of data, that is, roughly one spacecraft spin. Figure 3a shows a zoom in energy of the omnidirectional FPI ion spectrogram. The cold proton beam is observed intermittently at energies of 10–20 eV. A faint  $\text{He}^+$  beam is observed at  $\sim 80$  eV.  $V_{sc} \sim 10$  V is plotted on top (red). The ion energies plotted in Figure 3a correspond to the ones detected by the instrument, without any correction applied to account for the spacecraft potential. Therefore, their energy can be below the  $V_{sc}$  line, as is the case at 11:29:43 UT. The corresponding  $\mathbf{E} \times \mathbf{B}$  energy is plotted in blue. Its value is roughly 20 eV when the cold ions are detected. In the cold ion gap regions, the  $\mathbf{E}$  measurement is affected by  $\mathbf{E}_{\text{wake}}$ , and  $\mathbf{E} \times \mathbf{B}$  is not reliable. We computed partial ion moments from the FPI-DIS distribution functions for all ions with energies below 50 eV. The resulting cold ion density ( $n_{ic}$ ) is plotted in Figure 3b. Whenever the measured  $n_{ic}$  is larger than 50% of  $\max(n_{ic})$ , marked using a red line, the measurements are highlighted using \*. We use this criterion to define the cold ion gaps ( $n_{ic} < \max(n_{ic})/2$ ), marked with gray-shadowed areas, that is, the time intervals when FPI-DIS could not detect the cold ion beam. Figure 3c shows the cold ion velocity in GSE coordinates,

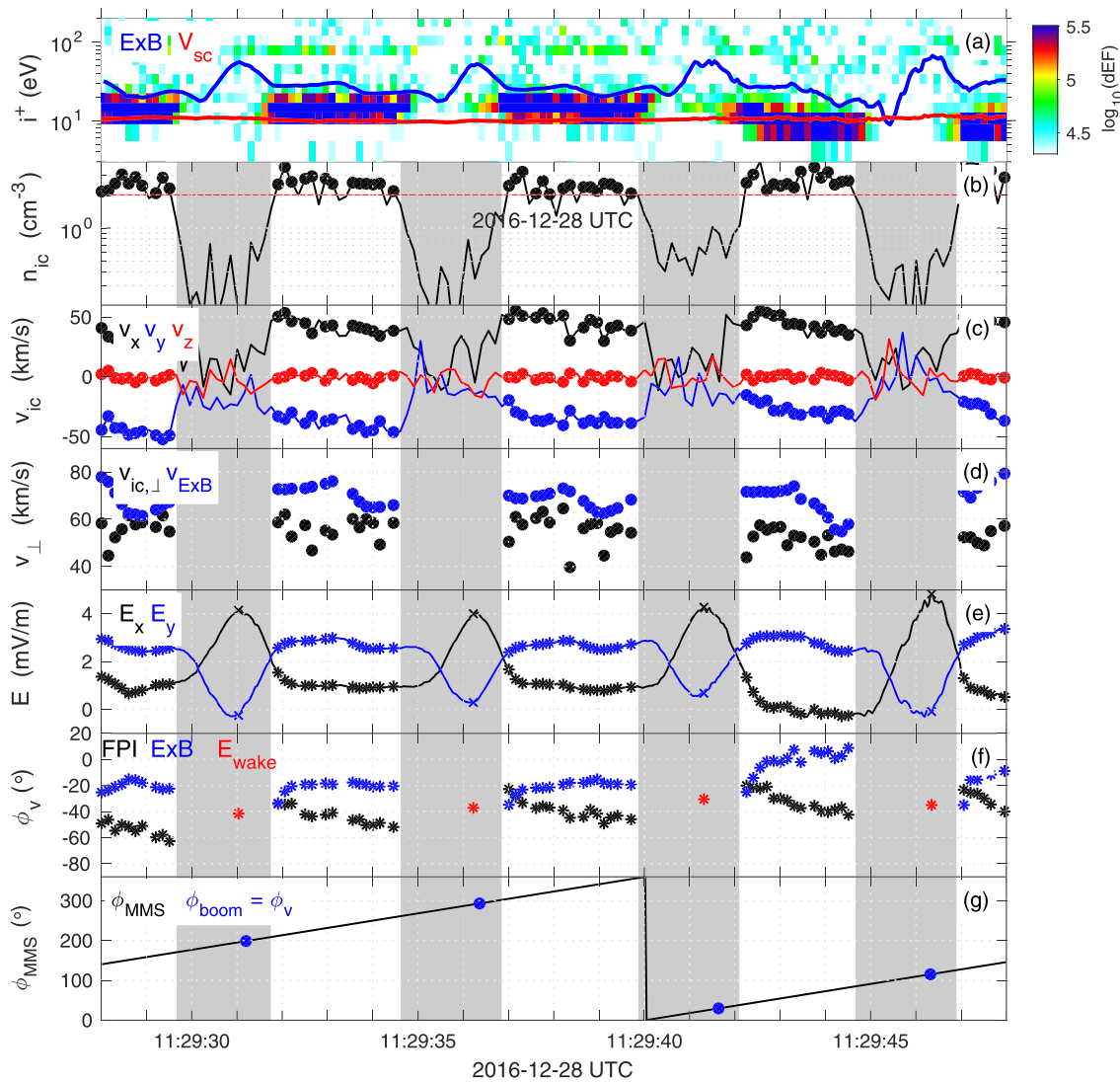


**Figure 3.** Detail of the cold ion beam gaps during one MMS spin. Gray-shadowed areas indicate the gaps in the cold ion beam detection, defined by a factor 2 decay in the measured cold ion density ( $n_{ic}$ ). (a; color) FPI ion spectrogram in dEF,  $\text{keV}/(\text{cm}^2 \text{ s sr keV})$ , (blue)  $\mathbf{E} \times \mathbf{B}$  energy for protons, (red) spacecraft potential ( $V_{sc}$ ),  $V$ . (b; black) FPI cold ion density ( $n_{ic}$ ), computed for all ions below 50 eV, (red) 50% level of the maximum  $n_{ic}$  measured in the interval of the figure. (c) FPI cold ion velocity ( $\mathbf{v}_{ic}$ , all ions below 50 eV) in GSE coordinates. (d; black) Perpendicular cold ion velocity, (blue) bulk ion velocity ( $\mathbf{v}_{E \times B}$ ). (e) Electric field in GSE coordinates, \* indicates regions where the cold ion beam reaches the spacecraft and  $\mathbf{E}$  is reliable,  $\times$  indicates the peak of  $\mathbf{E}_{wake}$ . (f) Estimates of the angle ( $\phi_v$ ) between GSE  $X$  axis and cold ion beam direction, projected on the spacecraft spin plane: (black) from  $\mathbf{v}_{ic}$ , (blue) from  $\mathbf{v}_{E \times B}$  and (red) from  $\mathbf{E}_{wake}$ . (g; black) MMS1 spin phase angle ( $\phi_{MMS}$ ), (blue)  $\phi_{MMS}$  whenever a wire boom is aligned with the cold ion beam direction, estimated from  $\mathbf{E}_{wake}$  ( $\phi_{boom} = \phi_v$ ). MMS = Magnetospheric MultiScale; dEF = differential energy flux; FPI = Fast Plasma Investigation.

obtained by calculating partial moments for all ions below 50 eV ( $\mathbf{v}_{ic}$ ). The regions where the cold ion beam was detected by FPI are marked using \*. The average cold ion velocity is  $\mathbf{v}_{ic} = [43, -35, 0.5]$  km/s when subtracting the cold ion gaps from the calculation, with a standard deviation of  $[7, 8.5, 2.5]$  km/s, indicating that the direction of the cold ion beam was relatively stable during the time interval of Figure 3. In Figure 3d, we compare the magnitude of the perpendicular bulk ion velocity taken from  $\mathbf{E} \times \mathbf{B}$  ( $\mathbf{v}_{E \times B}$ , blue) with  $\mathbf{v}_{ic,\perp}$  (black). If properly measured, the two terms should be in agreement when FPI detects the cold ion beam. However, we corrected for  $V_{sc}$  when computing  $\mathbf{v}_{ic}$ , assuming a spherical geometry of the spacecraft potential. It can be seen from Figure 1 that this approximation is not accurate. We attribute the deviation between  $\mathbf{v}_{E \times B}$  and  $\mathbf{v}_{ic,\perp}$  to inaccurate correction for the spacecraft potential. In addition, a residual  $\mathbf{E}_{wake}$  may be present in the regions where the cold ion beam is resolved by FPI, if a significant portion of the cold ion beam is still deflected by the potential structure. This is true, in particular, in the interval 11:29:42.5–11:29:47 UT,

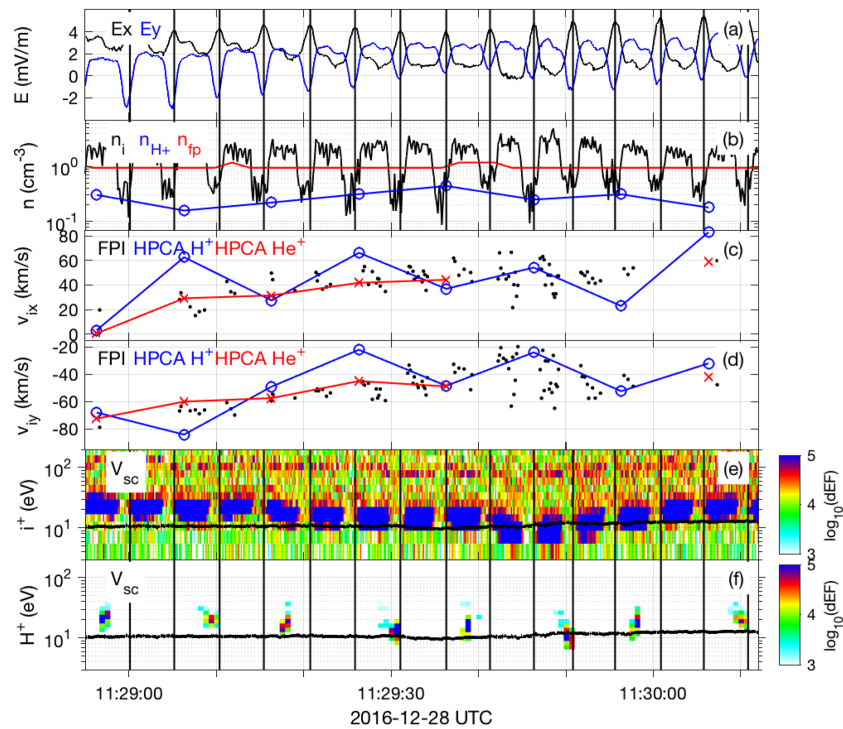


**Figure 4.** Comparison of FPI and HPCA observations of the cold ion beam (MMS1). Black vertical lines mark the time at which the  $\mathbf{E}$  field peaks, that is, is dominated by  $\mathbf{E}_{\text{wake}}$ . (a) Electric field in GSE coordinates. (b; black) Total ion density measured by FPI ( $n_i$ ), (blue) total  $\text{H}^+$  density measured by HPCA ( $n_{\text{H}^+}$ ), (red) density inferred from plasma frequency line observed by the electric field instrument ( $n_{\text{fp}}$ ). (c) GSE  $X$  component of the (black) FPI ion velocity, (blue) HPCA  $\text{H}^+$  velocity, and (red) HPCA  $\text{He}^+$  velocity. (d) GSE  $Y$  component of the (black) FPI ion velocity, (blue) HPCA  $\text{H}^+$  velocity, and (red) HPCA  $\text{He}^+$  velocity. (e; color) FPI ion spectrogram in dEF,  $\text{keV}/(\text{cm}^2 \text{ s sr keV})$ , (black) spacecraft potential ( $V_{\text{sc}}$ ),  $V$ . (f) (color) HPCA  $\text{H}^+$  subspin resolution spectrogram in dEF,  $\text{keV}/(\text{cm}^2 \text{ s sr keV})$ , (black) spacecraft potential ( $V_{\text{sc}}$ ),  $V$ . FPI = Fast Plasma Investigation; HPCA = Hot Plasma Composition Analyzer; MMS = Magnetospheric MultiScale; GSE = Geocentric Solar Ecliptic System; dEF = differential energy flux.

where the core of the cold ion beam is detected at energies below  $V_{\text{sc}}$ . Figure 3e shows the  $\mathbf{E}$  field measurement in GSE coordinates. The regions where the cold ion beam was detected by FPI are marked using \*. In the cold ion gap regions (i.e., not marked with \*), the measurement is strongly affected by  $\mathbf{E}_{\text{wake}}$ . Figure 3f shows the direction angle ( $\phi_v$ ) of the cold ion velocity in the plane perpendicular to the magnetic field (this plane roughly corresponds to the spin plane), where  $\phi_v = 0^\circ$  corresponds to the  $X_{\text{GSE}}$  direction and  $\phi_v = 90^\circ$  corresponds to the  $Y_{\text{GSE}}$  direction. It is obtained from three independent measurements: partial velocity moments from FPI ( $v_{\text{ic},\perp}$ , black), from  $\mathbf{v}_{\mathbf{E} \times \mathbf{B}}$  (blue), and from the direction of maximum  $\mathbf{E}_{\text{wake}}$  in the region where the  $\mathbf{E}$  field is dominated by the wake effect. The three methods show roughly consistent directions for the bulk ion velocity direction, with differences up to  $50^\circ$ . The disagreement becomes larger when the cold ion beam energy becomes smaller and closer to  $q_{\text{ic}} V_{\text{sc}}$ . Finally, we show the MMS1 spin phase ( $\phi_{\text{MMS}}$ , Figure 3g). The times when one of the four wire booms is aligned with the projection of  $\mathbf{v}_{\text{ic}}$  in the spin plane ( $\phi_{\text{boom}} = \phi_v$ ) are marked in blue and occur inside the gray-shadowed region (gap in cold ion beam detection by FPI-DIS). The FPI cold ion gap, however, is not centered at  $\phi_{\text{boom}} = \phi_v$  (blue marks). This is due to the way the FPI and SDP instruments are mounted in the MMS deck. We will come back to this point in section 4. The average angular width of the cold ion gaps observed by FPI is  $40.5^\circ$ .

### 3.2. Effects on the Hot Plasma Composition Analyzer

In this section, we compare the observations by FPI-DIS to the observations by HPCA during a subinterval of Figure 1 (11:28:55–11:30:15 UT), to assess to what degree HPCA is also affected by the potential structure of the spin-plane wire booms when resolving cold ion beams. Unlike FPI, HPCA relies on the spacecraft spin to compute a full 3-D sampling of the ion distribution functions, needing a half-spin ( $\sim 10$  s) to cover the full sky map. The field of view of the detector is  $11.25^\circ$  in azimuth and  $22.5^\circ$  in polar angle, with a total of 16 polar detectors covering  $360^\circ$ . HPCA is capable of detecting the time of flight of each particle, and

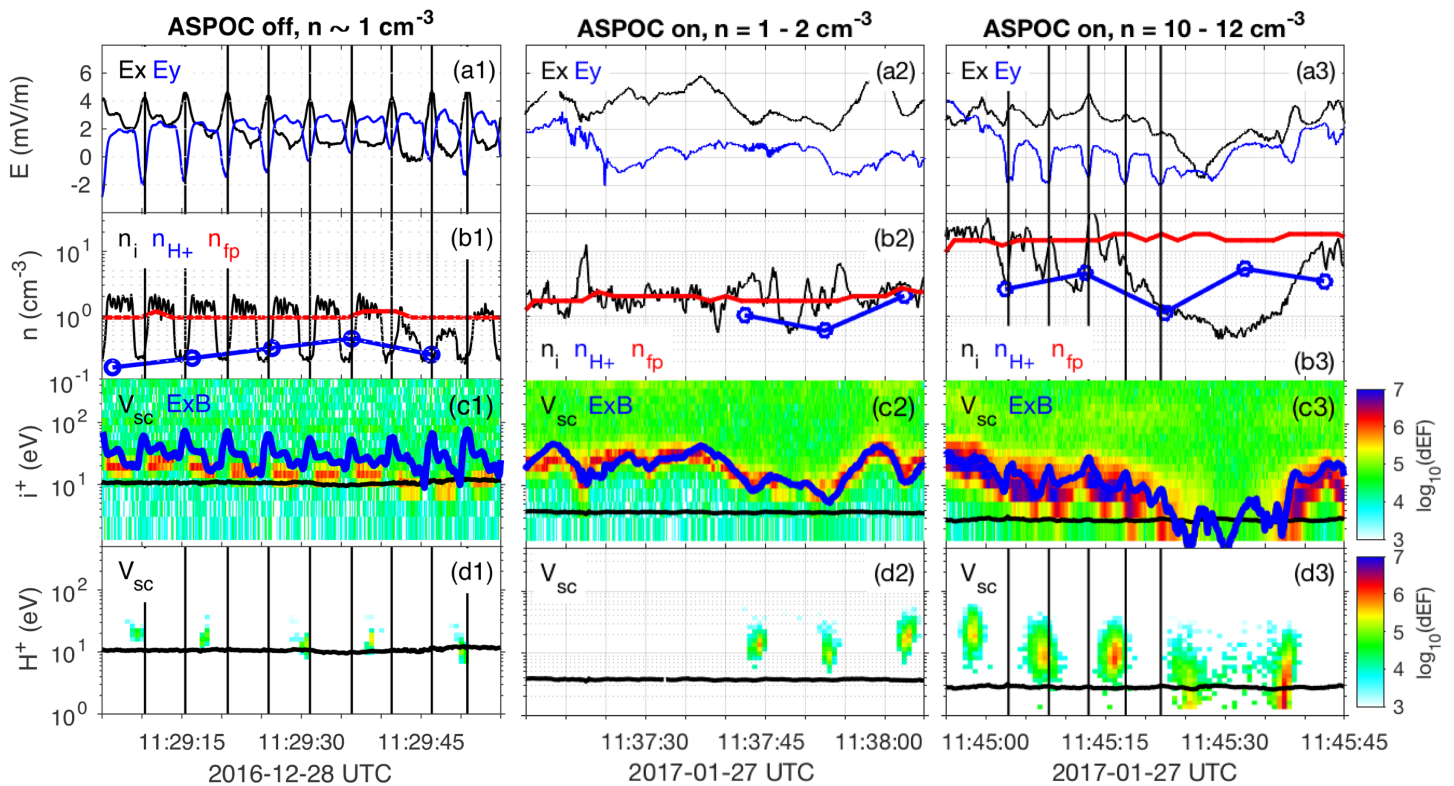


**Figure 5.** Comparison of three events (MMS1) where ASPOC is off/on and cold plasma density changes by an order of magnitude. Black vertical lines mark times of peak  $\mathbf{E}_{\text{wake}}$ . (a1–3) Electric field in GSE coordinates. (b1–3; black) Total ion density measured by FPI ( $n_i$ ), (blue) 50% total  $\text{H}^+$  density measured by HPCA ( $n_{\text{H}^+}$ ), (red) inferred from plasma frequency line observed by the electric field instrument ( $n_{\text{fp}}$ ). (c1–3; color) FPI ion spectrogram in dEF,  $\text{keV}/(\text{cm}^2 \text{ s sr keV})$ , (black line) spacecraft potential ( $V_{\text{sc}}$ ),  $\text{V}$ , (blue line)  $\mathbf{E} \times \mathbf{B}$  energy. (d1–3; color) HPCA  $\text{H}^+$  spectrogram in dEF  $\text{keV}/(\text{cm}^2 \text{ s sr keV})$ , (black line) spacecraft potential ( $V_{\text{sc}}$ ),  $\text{V}$ . MMS = Magnetospheric MultiScale; ASPOC = Active Spacecraft Potential Control; HPCA = Hot Plasma Composition Analyzer; dEF = differential energy flux.

therefore measure its mass. Figure 4a shows the  $X$  and  $Y$  GSE components of the electric field. It shows a periodicity of roughly 4.5 s, corresponding to  $\mathbf{E}_{\text{wake}}$ , each time one of the wire booms is aligned with the cold ion beam. The times of maximum  $\mathbf{E}_{\text{wake}}$  have been marked using vertical black lines. Figure 4b compares the plasma density measured by FPI-DIS ( $n_i$ , black), HPCA ( $n_{\text{H}^+}$ , blue) and inferred from the plasma frequency line measured by SDP ( $n_{\text{fp}}$ , red), as in Figure 2e. The FPI-DIS density is roughly a factor of 2 larger than the density estimated from the plasma frequency line, at times when there is no significant  $\mathbf{E}_{\text{wake}}$ . On the other hand, the HPCA density is a factor of 2–3 below, all the time. The temperature of the cold ion beam is of the order of 10 eV (inferred from computing partial moments of the FPI distribution function in the energy range 2–50 eV). HPCA, like all electrostatic analyzers, was calibrated with a beam in the laboratory that filled uniformly the whole angle-energy acceptance of the instrument. Therefore, for cold ion beams that do not fill this angle-energy acceptance, the geometric factor obtained from laboratory calibration is too large and the density derived from this geometric factor is too small. The degree to which the density is underestimated depends both on the beam temperature and its bulk velocity relative to the spacecraft, and therefore cannot be estimated in advance. Figures 4c and 4d compare the  $X$  and  $Y$  GSE components of the ion velocity ( $\mathbf{v}$ ), measured by FPI (black dots) and HPCA ( $\text{H}^+$ , blue, and  $\text{He}^+$ , red). The FPI-DIS-measured velocities, at times when the cold ion beam is not detected, have been masked. The three measurements are roughly in agreement. However, we note a  $\sim 10$ -s (half spin) fluctuation for the proton velocity measured by HPCA, that is not observed in  $\text{He}^+$ . We attribute this to a different effective electric field experienced by ions arriving to each of the fields of view of HPCA, as further detailed in the discussion section. Figure 4e shows the FPI ion spectrogram in dEF. The total energy of protons is of the order of the spacecraft potential ( $V_{\text{sc}}$ , black). A narrow ion beam roughly 4 times more energetic is also detected, corresponding to  $\text{He}^+$ . Figure 4f shows the HPCA proton spectrogram in dEF. Since HPCA needs a half spin to survey the 3-D skymap, the cold ion beam is observed every  $\sim 10$  s. The cold ion beam is observed at times when FPI cannot

**Table 1**  
Main Parameters of the Events in This Study

Event	Time	B	$\theta^a$	$n_{fp}^b$	$E \times B$	$T_{ic}$	$V_{sc}$	ASPOC <sup>c</sup>	
ID	Date	(UT)	(nT)	(°)	(cm <sup>-3</sup> )	(eV)	(V)	( $\mu$ A)	
2016	2016-12-28	11:29:30	43	11	0.6–0.9	31	<10	10.7	0
2017a	2017-01-27	11:37:40	64	7	1–2	21	<10	3.7	19.7
2017b	2017-01-27	11:45:20	65	10	10–12	13	<10	2.8	19.7

Notes. All quantities correspond to mean values during a 50-s interval centered at the reference time. Dates are formatted as YYYY-MM-DD

<sup>a</sup>Angle between magnetic field and spacecraft spin axis. <sup>b</sup>Plasma density estimated from plasma frequency. <sup>c</sup>ASPOC emitted current.

detect it (e.g., 11:29:30 UT, 11:29:50 UT), suggesting that at least one of the HPCA fields of view is less affected by the potential structure of the wire booms than for FPI-DIS. Details on the differences between the two HPCA fields of view will be discussed in section 4.

### 3.3. Mitigation Using Active Spacecraft Potential Control

The MMS fleet incorporates the Active Spacecraft Potential Control (ASPOC) instrument, consisting of an ion emitter that generates a current from the spacecraft toward the ambient plasma and reduces the charging of the spacecraft. During the event showed previously (28 December 2016, or simply 2016), the ASPOC was not in operation. We now show MMS measurements during another two events on 27 January 2017 (2017a and 2017b) of similar characteristics in terms of ambient plasma conditions, but with ASPOC on. This orbit has been recently studied by Cozzani et al. (2019), who reported an electron diffusion region encounter roughly 20 min after the intervals studied in Figure 5. A comparison between the main parameters of the events is given in Table 1. Most of the parameters are similar, with the exception of the ambient plasma density ( $n_{fp}$ ) which is 1 order of magnitude larger for event 2017b, and the ASPOC current, which was 0 for event 2016, reflected in a larger  $V_{sc}$ . The cold ion beams flow perpendicular to  $\mathbf{B}$ , owing to  $\mathbf{E} \times \mathbf{B}$  convection, and therefore the deflection by the wire boom potential structure will be large when the angle between background magnetic field and the spacecraft spin axis ( $\theta$ ) is small. In order to compare and assess the effect of the wire boom potential among the three events, it is important that this angle remains small and similar between the events (7–11° in the case studies of Table 1). In any case, this angle remains small most of the time when MMS is in the outer magnetosphere, owing to its equatorial orbit. The total kinetic energy of the cold ion beam depends on both its  $\mathbf{E} \times \mathbf{B}$  velocity and thermal energy ( $T_{ic}$ ), and it is important to have similar values among the events to compare the effect of the spacecraft potential structure as a function of ASPOC operation (2016 to 2017a) and plasma density (2017a to 2017b).

Figure 5 is divided into three columns (subscripts 1, 2 and 3) that correspond to events 2016, 2017a, and 2017b, respectively. As commented before, the main difference between event 2016 and 2017a is ASPOC off/on, and the main difference between 2017a and 2017b is the cold ion plasma density, which is an order of magnitude larger in event 2017b (both events have ASPOC on). Figures 5a1–5a3 show the spin plane electric field. Event 2016 (left) is contaminated by an intermittent  $\mathbf{E}_{wake}$  every quarter of spin period, event 2017a does not show clear  $\mathbf{E}_{wake}$ , and event 2017b is also affected by  $\mathbf{E}_{wake}$ . Figures 5b1–5b3 show the plasma density inferred from plasma frequency ( $n_{fp}$ , red), FPI-DIS ( $n_i$ , black), and HPCA ( $n_{H^+}$ , blue). We assume that  $n_{fp}$  is the best estimation of the true plasma density. The best agreement within the three plasma density measurements is found for event 2017a, that is, ASPOC on and a moderate amount of cold plasma. For event 2017b, despite ASPOC being on, the particle instruments provide low estimates of the plasma density on average (HPCA and FPI-DIS) and complex fluctuations of 1 order of magnitude which are not real (FPI-DIS). Figures 5c1–5c3 show FPI ion dEF (color), spacecraft potential ( $V_{sc}$ , black) and  $\mathbf{E} \times \mathbf{B}$  energy (blue).  $\mathbf{E} \times \mathbf{B}$  lines fluctuate for events 2016 and 2017b, owing to contamination by  $\mathbf{E}_{wake}$ . Figures 5d1–5d3 show HPCA proton dEF. HPCA detects protons in the regions close to maximum  $\mathbf{E}_{wake}$  (vertical black lines), indicating that HPCA is less affected by the wire boom potential structure.

The comparison between events 2016, 2017a, and 2017b indicates that ASPOC mitigates the effect of the spin-plane potential structure over FPI and HPCA measurements of the cold ion beam, for a moderate cold ion density. However, for dense beams such as the case presented in event 2017b, ASPOC on (emitting a current of 20  $\mu$ A) is not enough to fully resolve the cold ion beam. The particle detectors provide nonreal

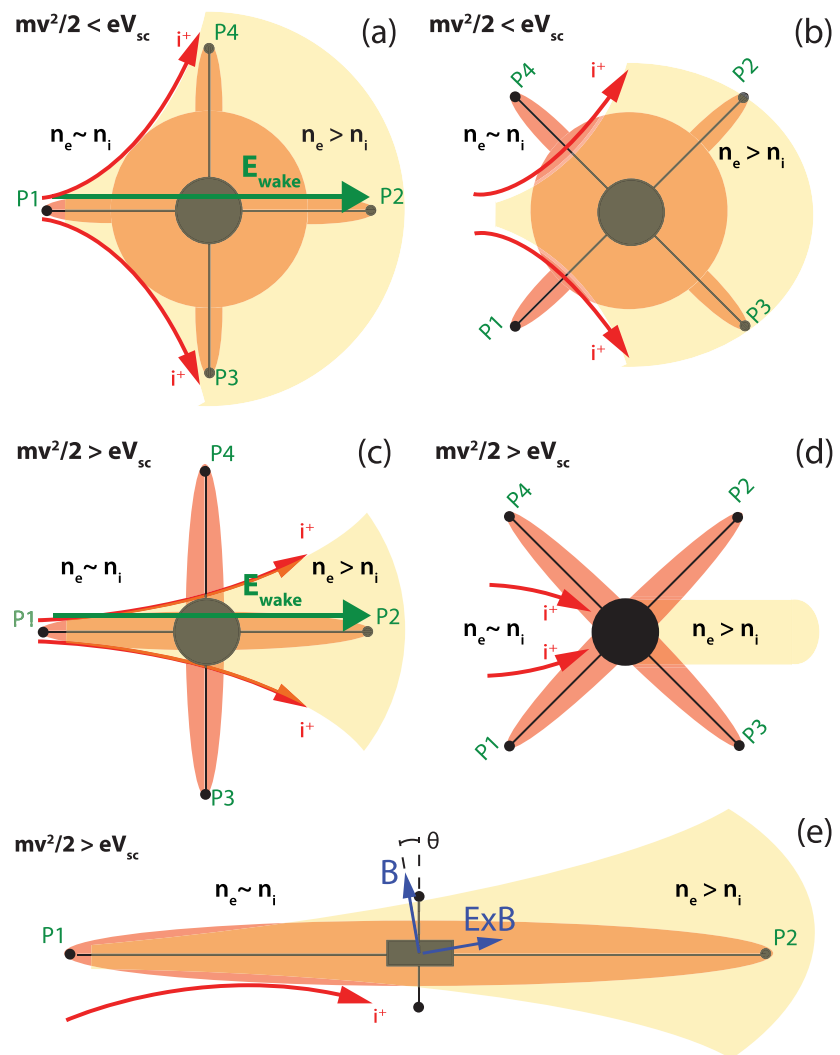


**Figure 6.** Sketches of the potential structure and ion wake formed around Magnetospheric MultiScale spacecraft. Spacecraft body and wake size are not to scale. (a) Cold ion deflection by the spacecraft body and spin-plane booms potential structure (red-shadowed region), case  $mv_{ic}^2/2 < q_{ic}V_{sc}$ . An enhanced ion wake is formed (yellow-shadowed region). (b) Same as (a) without alignment between the ion beam and electric field booms, a smaller ion wake (yellow-shadowed region) is formed than for case (a), owing to the spacecraft body potential structure. (c) Cold ion deflection by the spacecraft potential structure (red-shadowed region), case  $mv_{ic}^2/2 > q_{ic}V_{sc}$ . A narrow, boom-induced ion wake is formed behind the spacecraft (yellow-shadowed region). (d) Same as (c) without alignment between the ion beam and electric field booms. The cold ions are focused toward the spacecraft by the effect of the spin-plane booms. A narrow wake is formed behind the spacecraft, mainly the region blocked by the spacecraft body (yellow-shadowed region, note that the spacecraft body and therefore the wake behind it are not to scale in this plot, but magnified for better visualization). (e) View from the side of the narrow, boom-induced ion wake.

fluctuations (FPI-DIS) and low estimates of the cold ion density (FPI-DIS and HPCA), and wake electric fields are present.

#### 4. Discussion and Conclusion

In Figure 6, we show diagrams of the spacecraft potential structure and the ion wake formed, owing to cold ion beams under different situations. The size of the spacecraft body is not to scale, to better illustrate its effects. Since the scale size of both the spacecraft and the booms is below the Debye length-scale, a rarefaction of cold ions (wake) is formed behind the spacecraft when the cold ion flow is supersonic ( $mv_{ic}^2/2 > KT_{ic}$ ), a common situation in the magnetosphere. Electrons, on the other hand, are not supersonic, owing to their smaller mass, and no electron wake is formed. This charge imbalance generates a local  $\mathbf{E}$  field from probe 1

to probe 2, or  $E_{\text{wake}}$  (see Figure 6a). The size and magnitude of the ion wake behind the spacecraft depends on the ratio between the cold ion beam bulk kinetic energy and  $q_{ic}V_{sc}$ . If the bulk kinetic energy of the cold ion beam is below the equivalent spacecraft potential ( $mv_{ic}^2/2 < q_{ic}V_{sc}$ ), the potential structure of the spacecraft body (red-shadowed areas around spacecraft body in Figures 6a and 6b) has a strong effect over the ion beam, deflecting it and preventing it from reaching the spacecraft (Engwall et al., 2006). This is the situation in the interval 11:28:20–11:28:40 UT of Figure 2, where no cold ions are detected by FPI (small interval in the center of Figure 2f). Under this situation, an enhanced wake is formed behind the spacecraft (yellow-shadowed regions in Figures 6a and 6b). The effect of the potential structure caused by the electric field booms (red-shadowed areas around the booms) is less important, and a large wake is formed for all angles between the ion beam and the orientation of the booms (see  $E_{\text{wake}}$  measurement in Figure 2c). However, the size of the wake is modulated by the additional effect of the booms when they are aligned with the beam further enhancing the size of the wake. The electric field instrument is affected by  $E_{\text{wake}}$  throughout the whole spin period, and its magnitude fluctuates over that period, becoming maximal each time one of the booms is aligned with the cold ion beam, and reaching a minimum in between the alignments. For the time interval mentioned above, 11:28:20–11:28:40 UT of Figure 2, the  $E_{\text{wake}}$  magnitude is  $> 3$  mV/m when the beam is aligned with each of the spin-plane booms, and goes down to less than 1 mV/m in between (not shown).

Figures 6c–6e show the situation when the bulk kinetic energy of the ion beam exceeds the equivalent spacecraft potential ( $mv_{ic}^2/2 > q_{ic}V_{sc}$ ), as it occurs in the three events shown in this work (Figures 3, 4 and 5). In this case, the effect of the spacecraft body potential structure is less important. It still modifies the bulk kinetic energy and direction of the ion beam, but the ions can penetrate this potential structure, reach the ion detectors, and no enhanced wake is formed behind the spacecraft. In this case, the relative orientation between the electric field booms and the ion beam becomes much more important. For a thin wire, the radial electric field decays inversely proportional to the distance to the wire ( $1/r$ ), instead of ( $1/r^2$ ) as is the case for a sphere (Cully et al., 2007). When the ion beam and the booms are aligned (Figure 6c), the ion beam experiences a radial electric field along its path flowing parallel to the boom, and generates a wake behind the spacecraft (yellow-shadowed). We term this effect *boom-induced wake electric field*, and it corresponds to the situation in the gray-shadowed regions of Figure 3. If we assume the cold ion beam velocity is constant over one spacecraft spin time interval, then the effect will be observed roughly every quarter of a spin. The boom-induced wake is narrower than the classical or enhanced wake described above, and its size and intensity depend mainly on  $V_{sc}$ ,  $v_{ic}$  and the length of the booms. When the cold ion beam and the booms are not aligned (Figure 6d), the ion beam is affected in a different way by the electric field, coming from the spin-plane booms potential structure. Under these circumstances, the cold ion beam may be funneled toward the spacecraft by the boom potential structure (Miyake et al., 2013). This effect is consistent with the overestimation of the ion density that FPI observes ( $n_i$ ) at some portions of the spin (see Figures 2e and 4b). A very narrow wake behind the spacecraft body is still formed, but this wake is smaller than for situations illustrated in Figures 6a–6c. Note that the size of the spacecraft body (and therefore the wake width in Figure 6d) are not to scale, but magnified for visualization purposes. The sketch of Figure 6d corresponds to the situation in the white-shadowed regions of Figure 3. Figure 6e shows a side view of the boom-induced wake effect, which is larger when the cold ion beam velocity is contained in the spin plane, or, in other words, the magnetic field forms a small angle with the spacecraft spin axis ( $\theta$ ). This is a common situation for MMS in the dayside magnetosphere, owing to its nearly equatorial orbit and spin axis pointing roughly in Z GSE. For the events discussed in this work, the angle  $\theta$  varied between  $7^\circ$  and  $11^\circ$  (see Table 1).

For MMS, the importance of the boom-induced wake reported here ( $mv_{ic}^2/2 > q_{ic}V_{sc}$ ) depends mainly on the following parameters: spacecraft potential, bulk kinetic and thermal energy of the cold ion beam, angle between the magnetic field and the spin axis ( $\theta$ , see Figure 6e), and ASPOC operations. The example shown in Figure 2 is very illustrative, and such clear signatures are not often observed. However, we expect boom-induced wake effects on electric field and particle measurements in the magnetosphere whenever the angle between the magnetic field and the spin axis is small, and the bulk kinetic energy exceeds the equivalent spacecraft potential and the thermal energy of the cold ion beam. This is true for MMS most of the time on the magnetospheric side of the Earth's magnetopause. However, if the bulk kinetic energy of the ion beam is much larger than  $q_{ic}V_{sc}$ , the effect will be small. ASPOC reduces  $V_{sc}$  by a factor 3–4, and therefore this effect is mitigated when ASPOC is operating.

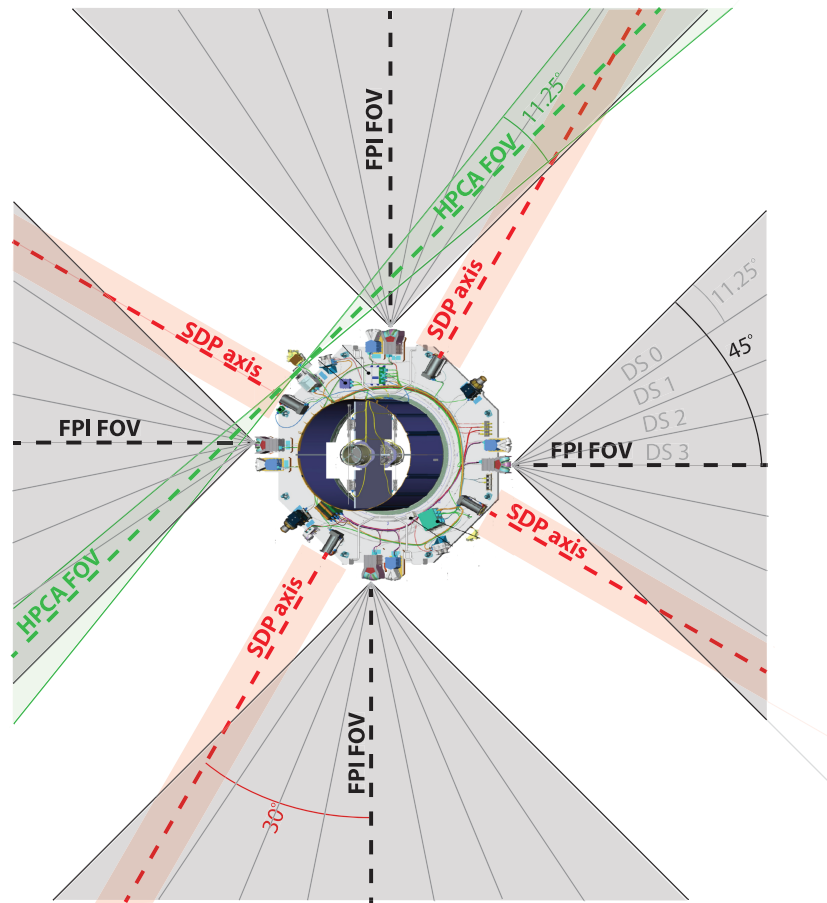


**Figure 7.** Detail of FPI-DIS and HPCA fields of view, and SDP deployment on Magnetospheric MultiScale (adapted from Burch et al., 2015). FPI relies on 32 deflection states (DS) in azimuth to accomplish full sky coverage every 160 ms. HPCA relies on spacecraft spin and covers the full skymap every half spin ( $\sim 10$  s). One of the fields of view is more affected by the SDP boom potential structure than the other. FPI = Fast Plasma Investigation; FPI-DIS = FPI Dual Ion spectrometers; HPCA = Hot Plasma Composition Analyzer; FOV = field of view; SDP = Spin Double Probes.

In Figure 7, we plot the fields of view of the FPI-DIS dual spectrometers and HPCA, as well as the deployment of the SDP booms. It can be seen that the SDP booms directly block part of the fields of view of the dual FPI-DIS in the spin plane, each at a  $30^\circ$  angle with one of the SDP booms. HPCA, unlike FPI, relies on the spacecraft spin to complete a full 3-D survey of the sky, and its field of view consists of two antiparallel and narrow ( $11.25^\circ$  in azimuth each) regions of the sky. As can be seen in the diagram of Figure 7, one of the field-of-view directions of HPCA (top HPCA FOV in Figure 7) is more affected than the other by the electric field booms potential structure, because it directly crosses with one of the booms. In Figures 4c and 4d we showed that the measured proton velocity by HPCA was fluctuating every 10 s, that is, each of the fields of view of HPCA measured a different proton velocity. We propose that this effect is due to an asymmetric effect of the spacecraft potential to each field of view.

Cold ion wakes generated in the vicinity of charged spacecraft are an unwanted effect that makes particle and field measurements operate in unconventional ways that are more difficult to interpret. However, some information can be extracted from the cold ion beam when it is deviated by the spacecraft potential. Engwall et al. (2008) used the wake effect observed by the Cluster spacecraft (Escoubet et al., 2001), in combination with particle drift instrumentation, to measure the background electric field, to infer the flux of invisible cold ions in the magnetotail lobes. André and Cully (2012) used the same technique over a larger Cluster spacecraft dataset and revised upward the number density of cold ions in the Earth's magnetosphere. However, particle drift instruments are complicated to operate, and these measurements are not always available. Some constraints on the cold ion component can still be inferred by combining particle measurements and

electric field measurements from double probes without the need for particle drift measurements. If a wake is detected and no cold ions are observed throughout a spin, then we can conclude the existence of a supersonic ion beam with both its kinetic and thermal energy below the spacecraft potential equivalent energy  $q_{ic}V_{sc} > mv_{ic}^2/2 > KT_{ic}$ . On the other hand, if the cold ion beam is detected but fluctuating over a spin period, similar to Figure 2, then we can conclude that  $mv_{ic}^2/2 > q_{ic}V_{sc} > KT_{ic}$ . Note also that in most situations,  $v_{ic} = v_{E \times B}$ . Under the two situations, the direction of  $v_{ic}$  can be extrapolated from the direction of  $\mathbf{E}_{wake}$  (see Figure 3f). The  $\mathbf{E}_{wake}$  magnitude depends on the ion beam flux (density and velocity), and it is possible to constrain the flux of the ion beam using the electric field measurement, but calibrating this effect would require a large number of events with varying fluxes, and it is left for future work.

One of the implications of the findings presented here is that statistical surveys of the cold ionospheric component in the magnetosphere that rely on particle instruments (e.g., Chen & Moore, 2006; Fuselier et al., 2017; Lee & Angelopoulos, 2014) will routinely provide biased estimates of the cold ion density, even if active potential control mechanisms are present. The results of these surveys need to be considered as lower thresholds for the true amount of cold plasma of ionospheric origin. Indirect measurements using the wake method (André & Cully, 2012; André et al., 2015; Li et al., 2013) provide larger densities in most parts of the magnetosphere.

To summarize, the cold ion component of ionospheric origin that is present most of the time in most of the regions of the magnetosphere is difficult to characterize by in situ measurements using particle detectors, because the nonspherical potential structure around spacecraft alters both the trajectory and energy of cold ions. Particle measurements are usually corrected for spacecraft potential effects, assuming a spherically symmetric potential structure of the spacecraft body (corresponding to a radial electric field). This approximation is not valid for particles with thermal or drift energies close to the spacecraft potential, which are strongly affected by the electrostatic potential structure of spacecraft booms. For the MMS examples presented in this work, active control of spacecraft potential helps to mitigate these effects for moderate beam plasma density ( $n_{ic} \sim 1 \text{ cm}^{-3}$ ), but we show that the cold population is underestimated with ASPOC on (ASPOC current is 20  $\mu\text{A}$ ) for an event with a large beam plasma density ( $n_{ic} \sim 10 \text{ cm}^{-3}$ ). These types of events, featuring dense cold ion beams, may benefit from ASPOC operating at higher current range. Maintaining  $V_{sc}$  as low as possible is crucial for resolving cold ion beams in the magnetosphere. When cold ions are deflected by the potential structure, an ion rarefaction is formed behind the spacecraft that affects electric field measurements. Understanding the electromagnetic environment surrounding the spacecraft helps us to understand these kind of measurements and enables indirect techniques for detecting the cold plasma components and inferring their main characteristics, such as density, velocity and temperature.

#### Acknowledgments

We acknowledge support from the ISSI international team *Cold plasma of ionospheric origin in the Earth's magnetosphere* and from the ESA science faculty. Research at IRAP was supported by CNRS, CNES, and the University of Toulouse. STR acknowledges support of the Ministry of Economy and Competitiveness (MINECO), Spain, grant No. FIS2017-90102-R. Research at Southwest Research Institute is supported by the prime NASA MMS contract. MMS data are publicly available online (at <https://lasp.colorado.edu/mms/sdc/public/>).

#### References

- André, M., & Cully, C. M. (2012). Low-energy ions: A previously hidden solar system particle population. *Geophysical Research Letters*, *39*, L03101. <https://doi.org/10.1029/2011GL050242>
- André, M., Li, K., & Eriksson, A. I. (2015). Outflow of low-energy ions and the solar cycle. *Journal of Geophysical Research: Space Physics*, *120*, 1072–1085. <https://doi.org/10.1002/2014JA020714>
- Andriopoulou, M., Nakamura, R., Torkar, K., Baumjohann, W., & Hoelzl, B. (2015). Deriving plasma densities in tenuous plasma regions, with the spacecraft potential under active control. *Journal of Geophysical Research: Space Physics*, *120*, 9594–9616. <https://doi.org/10.1002/2015JA021472>
- Bergman, S., Stenberg Wieser, G., Wieser, M., & Johansson, F. (2018). Correction of low-energy ion measurements from Rosetta-ICA for the effects of spacecraft charging. *European Planetary Science Congress*, EPSC Abstracts Vol. 12, EPSC2018-230. Berlin, Germany.
- Burch, J. L., Moore, T. E., Torbert, R. B., & Giles, B. L. (2015). Magnetospheric Multiscale overview and science objectives. *Space Science Reviews*, *199*(1–4), 5–21.
- Chappell, C. R. (2015). The role of the ionosphere in providing plasma to the terrestrial magnetosphere—An historical overview. *Space Science Reviews*, *192*(1–4), 5–25.
- Chen, S. H., & Moore, T. E. (2006). Magnetospheric convection and thermal ions in the dayside outer magnetosphere. *Journal of Geophysical Research*, *111*, A03215. <https://doi.org/10.1029/2005JA011084>
- Cipriani, F. (2016). Simulation of the electrostatic environment of the Magnetospheric Multiscale mission using the Active Spacecraft Potential Control System. In *14th SCTC—Spacecraft Charging Technology Conference*, 1. Noordwijk, The Netherlands.
- Cipriani, F., Escoubet, C. P., Torkar, K., Nakamura, R., Deprez, G., Rodgers, D., & Barrie, A. (2018). Simulated effects of ASPOCS on plasma measurements performed onboard the magnetospheric multiscale mission. In *15th SCTC—Spacecraft Charging Technology Conference*. Kobe, Japan.
- Cozzani, G., Retino, A., Califano, F., Alexandrova, A., Contel, O. L., Khotyaintsev, Y., & Burch, J. L. (2019). In situ spacecraft observations of a structured electron diffusion region during magnetopause reconnection. *Physical Review E*, *99*, 4.
- Cully, C. M., Ergun, R. E., & Eriksson, A. I. (2007). Electrostatic structure around spacecraft in tenuous plasmas. *Journal of Geophysical Research*, *112*, A09211. <https://doi.org/10.1029/2007JA012269>
- Dandouras, I. (2013). Detection of a plasmaspheric wind in the Earth's magnetosphere by the Cluster spacecraft. *Annales Geophysicae*, *31*(7), 1143–1153.

- Darrouzet, F., Gallagher, D. L., André, N., Carpenter, D. L., Dandouras, I., Décréau, M. E., & Tu, J. (2008). Plasmaspheric density structures and dynamics: Properties observed by the CLUSTER and IMAGE missions. *Space Science Reviews*, *145*(1-2), 55–106.
- Engwall, E., Eriksson, A. I., André, M., Dandouras, I., Paschmann, G., Quinn, J., & Torkar, K. (2006). Low-energy (order 10 eV) ion flow in the magnetotail lobes inferred from spacecraft wake observations. *Geophysical Research Letters*, *33*, L06110. <https://doi.org/10.1029/2005GL025179>
- Engwall, E., Eriksson, A. I., Cully, C. M., Andre, M., Puhl-Quinn, P. A., Vaith, H., & Torbert, R. (2009). Survey of cold ionospheric outflows in the magnetotail. *Annales Geophysicae*, *27*(8), 3185–3201.
- Engwall, E., Eriksson, A. I., Cully, C. M., André, M., Torbert, R., & Vaith, H. (2008). Earth's ionospheric outflow dominated by hidden cold plasma. *Nature Geoscience*, *2*(1), 24–27.
- Ergun, R. E., Tucker, S., Westfall, J., Goodrich, K. A., Malaspina, D. M., Summers, D., & Cully, C. M. (2014). The axial double probe and fields signal processing for the MMS mission. *Space Science Reviews*, *199*(1-4), 167–188.
- Escoubet, C. P., Fehringer, M., & Goldstein, M. (2001). The Cluster mission—Introduction. *Annales Geophysicae*, *19*(10-12), 1197–1200.
- Fuselier, S. A., Burch, J. L., Mukherjee, J., Genestreti, K. J., Vines, S. K., Gomez, R., & Strangeway, R. J. (2017). Magnetospheric ion influence at the dayside magnetopause. *Journal of Geophysical Research: Space Physics*, *122*, 8617–8631. <https://doi.org/10.1002/2017JA024515>
- Gustafsson, G., Bostrom, R., Holback, B., Holmgren, G., Lundgren, A., Stasiewicz, K., & Wygant, J. (1997). The electric field and wave experiment for the Cluster mission. *Space Science Reviews*, *79*(1-2), 137–156.
- Hirahara, M., Seki, K., Saito, Y., & Mukai, T. (2004). Periodic emergence of multicomposition cold ions modulated by geomagnetic field line oscillations in the near-Earth magnetosphere. *Journal of Geophysical Research*, *109*, A03211. <https://doi.org/10.1029/2003JA010141>
- Lavraud, B., & Larson, D. E. (2016). Correcting moments of in situ particle distribution functions for spacecraft electrostatic charging. *Journal of Geophysical Research: Space Physics*, *121*, 8462–8474. <https://doi.org/10.1002/2016JA022591>
- Le Contel, O., Leroy, P., Roux, A., Coillot, C., Alison, D., Bouabdellah, A., et al. (2014). The Search-Coil Magnetometer for MMS. *Space Science Reviews*, *199*(1-4), 257–282.
- Lee, J. H., & Angelopoulos, V. (2014). On the presence and properties of cold ions near Earth's equatorial magnetosphere. *Journal of Geophysical Research: Space Physics*, *119*, 1749–1770. <https://doi.org/10.1002/2013JA019305>
- Li, K., Haaland, S., Eriksson, A., André, M., Engwall, E., Wei, Y., & Ren, Q. Y. (2013). Transport of cold ions from the polar ionosphere to the plasma sheet. *Journal of Geophysical Research: Space Physics*, *118*, 5467–5477. <https://doi.org/10.1002/jgra.50518>
- Lindqvist, P. A., Olsson, G., Torbert, R. B., King, B., Granoff, M., Rau, D., & Tucker, S. (2014). The Spin-Plane Double Probe Electric Field Instrument for MMS. *Space Science Reviews*, *199*(1-4), 137–165.
- McFadden, J. P., Carlson, C. W., Larson, D., Bonnell, J., Mozer, F. S., Angelopoulos, V., & Auster, U. (2008). Structure of plasmaspheric plumes and their participation in magnetopause reconnection: First results from THEMIS. *Geophysical Research Letters*, *35*, L17S10. <https://doi.org/10.1029/2008GL033677>
- Miyake, Y., Cully, C. M., Usui, H., & Nakashima, H. (2013). Plasma particle simulations of wake formation behind a spacecraft with thin wire booms. *Journal of Geophysical Research: Space Physics*, *118*, 5681–5694. <https://doi.org/10.1002/jgra.50543>
- Miyake, Y., & Usui, H. (2016). Particle-in-cell modeling of spacecraft-plasma interaction effects on double-probe electric field measurements. *Radio Science*, *51*, 1905–1922. <https://doi.org/10.1002/2016RS006095>
- Olsen, R. C. (1982). The hidden ion population of the magnetosphere. *Journal of Geophysical Research*, *87*(A5), 3481–3488.
- Paulsson, J. J. P., Spicher, A., Clausen, L. B. N., Moen, J. I., & Miloch, W. J. (2018). Wake potential and wake effects on the ionospheric plasma density measurements with sounding rockets. *Journal of Geophysical Research: Space Physics*, *123*, 9711–9725. <https://doi.org/10.1029/2017JA025004>
- Pedersen, A., Cattell, C. A., Falthammar, C. G., Formisano, V., Lindqvist, P. A., Mozer, F., & Torbert, R. (1984). Quasistatic electric-field measurements with spherical double probes on the geos and isee satellites. *Space Science Reviews*, *37*(3-4), 269–312.
- Pollock, C., Moore, T., Jacques, A., Burch, J., Gliese, U., Saito, Y., & Zeuch, M. (2016). Fast plasma investigation for Magnetospheric Multiscale. *Space Science Reviews*, *199*(1-4), 331–406.
- Roussel, J. F., Rogier, F., Dufour, G., Mateo-Velez, J. C., Forest, J., Hilgers, A., & Payan, D. (2008). SPIS open-source code: Methods, capabilities, achievements, and prospects. *IEEE Transactions on Plasma Science*, *36*(5), 2360–2368.
- Russell, C. T., Anderson, B. J., Baumjohann, W., Bromund, K. R., Dearborn, D., Fischer, D., & Richter, I. (2014). The Magnetospheric Multiscale Magnetometers. *Space Science Reviews*, *199*(1-4), 189–256.
- Sauvaud, J. A., Lundin, R., Reme, H., McFadden, J. P., Carlson, C., Parks, G. K., & McCarthy, M. (2001). Intermittent thermal plasma acceleration linked to sporadic motions of the magnetopause, first Cluster results. *Annales Geophysicae*, *19*(10-12), 1523–1532.
- Su, Y. J., Horwitz, J. L., Moore, T. E., Giles, B. L., Chandler, M. O., Craven, P. D., & Pollock, C. J. (1998). Polar wind survey with the Thermal Ion Dynamics Experiment Plasma Source Instrument suite aboard POLAR. *Journal of Geophysical Research*, *103*(A12), 29,305–29,337.
- Szita, S., Fazakerley, A. N., Carter, P. J., James, A. M., Travnick, P., Watson, G., & Torkar, K. (2001). Cluster PEACE observations of electrons of spacecraft origin. *Annales Geophysicae*, *19*(10-12), 1721–1730.
- Toledo-Redondo, S., André, M., Khotyaintsev, Y. V., Lavraud, B., Vaivads, A., Graham, D. B., & Burch, J. L. (2017). Energy budget and mechanisms of cold ion heating in asymmetric magnetic reconnection. *Journal of Geophysical Research: Space Physics*, *122*, 9396–9413. <https://doi.org/10.1002/2017JA024553>
- Toledo-Redondo, S., Vaivads, A., André, M., & Khotyaintsev, Y. V. (2015). Modification of the Hall physics in magnetic reconnection due to cold ions at the Earth's magnetopause. *Geophysical Research Letters*, *42*, 6146–6154. <https://doi.org/10.1002/2015GL065129>
- Torkar, K., Nakamura, R., Tajmar, M., Scharlemann, C., Jeszenszky, H., Laky, G., & Svenes, K. (2014). Active spacecraft potential control investigation. *Space Science Reviews*, *199*(1-4), 515–544.
- Torkar, K., Riedler, W., Escoubet, C. P., Fehringer, M., Schmidt, R., Grard, R. J. L., & Zhao, H. (2001). Active spacecraft potential control for Cluster—Implementation and first results. *Annales Geophysicae*, *19*(10-12), 1289–1302.
- Yau, A. W., & Andre, M. (1997). Sources of ion outflow in the high latitude ionosphere. *Space Science Reviews*, *80*(1-2), 1–25.
- Young, D. T., Burch, J. L., Gomez, R. G., De Los Santos, A., Miller, G. P., Wilson, P., & Webster, J. M. (2014). Hot plasma composition analyzer for the Magnetospheric Multiscale mission. *Space Science Reviews*, *199*(1-4), 407–470.